

On the importance of path for phase unwrapping in synthetic aperture radar interferometry

Batuhan Osmanoglu,^{1,*} Timothy H. Dixon,^{1,2}
Shimon Wdowinski,¹ and Enrique Cabral-Cano³

¹University of Miami, Rosenstiel School of Marine & Atmospheric Science-Marine Geology and Geophysics,
4600 Rickenbacker Causeway, Miami, Florida 33149, USA

²Currently at the Department of Geology, University of South Florida,
4202 East Fowler Avenue, Tampa, Florida 33620, USA

³Departamento de Geomagnetismo y Exploración, Instituto de Geofísica, Universidad Nacional
Autónoma de México, Ciudad Universitaria, Mexico D.F. 04510, Mexico

*Corresponding author: batu@rsmas.miami.edu

Received 5 October 2010; revised 21 March 2011; accepted 22 March 2011;
posted 28 March 2011 (Doc. ID 135309); published 23 June 2011

Phase unwrapping is a key procedure in interferometric synthetic aperture radar studies, translating ambiguous phase observations to topography, and surface deformation estimates. Some unwrapping algorithms are conducted along specific paths based on different selection criteria. In this study, we analyze six unwrapping paths: line scan, maximum coherence, phase derivative variance, phase derivative variance with branch-cut, second-derivative reliability, and the Fisher distance. The latter is a new path algorithm based on Fisher information theory, which combines the phase derivative with the expected variance to get a more robust path, potentially performing better than others in the case of low image quality. In order to compare only the performance of the paths, the same unwrapping function (phase derivative integral) is used. Results indicate that the Fisher distance algorithm gives better results in most cases. © 2011 Optical Society of America

OCIS codes: 280.6730, 100.5088.

1. Introduction

Interferometric synthetic aperture radar (InSAR) phase change measurements have been used to study earthquake and magmatic induced crustal deformation [1–5], subsidence due to ground water extraction and mining [6–9], glacial ice flow [10], and wetland water level changes [11,12]. Phase values are defined between $-\pi$ and $+\pi$, and observations that capture a signal with a larger dynamic range require phase unwrapping.

In the past three decades, several phase unwrapping algorithms have been developed. Some of these algorithms unwrap along a defined path, usually

based on a cost (or quality) function or geometrical relations. Other unwrapping methods try to minimize a misfit function globally without following a path. However, there have been few studies that focus on the importance of the path algorithm. In this paper, we review previous work on unwrapping with an emphasis on path, discuss five commonly used paths, and introduce a new path algorithm based on the Fisher information theory. We then compare the results of these algorithms in a variety of test cases and point out similarities and differences. The focus of this paper is on the unwrapping path rather than the unwrapping algorithm, evaluation of the circumstances (geometric baseline, noise, aliasing, etc.) where these paths are likely to fail, and evaluation of which paths have a tendency to propagate error.

2. Background

Single polarization synthetic aperture radar (SAR) provides two observables: amplitude and phase. Amplitude is proportional to the strength of the signal scattered back to the satellite from a target and can be used to create a black-and-white radar image. The phase observable mainly reflects the distance between the target and the satellite [13], but is also affected by atmospheric moisture conditions and other measurement noise. With two or more SAR acquisitions, it is possible to exploit differential phase information to estimate topography (digital elevation models [DEM]) or surface displacement.

Repeat-pass interferometric phase measurements are constructed by subtracting the phase of the second (slave) image from the first (master) image. Because the images are taken at different times from the repeating orbits, the satellites are not at the same exact location creating a baseline (spatial difference in satellite location). Interferometric phase can be defined as

$$\phi_I = \phi_M - \phi_S = \frac{4\pi(R_M - R_S)}{\lambda}, \quad (1)$$

where ϕ is the phase, R is the range, λ indicates the radar wavelength and subscripts I , M , and S stand for the interferogram, master, and slave [14]. Phase values are observed modulo 2π , causing range changes larger than $\lambda/2$ to be aliased. For most applications, the total amount of displacement is required. Phase unwrapping is the operation to remove the ambiguity from the phase observations, converting ambiguous phase change to unambiguous range change. The presence of noise, decorrelation effects, aliasing, and radar shadow complicate the unwrapping procedure. In multipass interferometry, there are several decorrelation sources: (1) baseline decorrelation (γ_{baseline}), (2) temporal decorrelation (γ_{temporal}), (3) Doppler centroid decorrelation (γ_{Doppler}), (4) volume decorrelation (γ_{volume}), (5) thermal decorrelation (γ_{thermal}), and (6) processing related decorrelation ($\gamma_{\text{processing}}$) [15]. In addition to decorrelation effects, orbital errors (γ_{orbit}) and atmospheric phase contributions ($\gamma_{\text{atmosphere}}$) also affect the interferometric phase measurements. The combined effect of these decorrelation sources is multiplicative, as follows:

$$\gamma_{\text{total}} = \gamma_{\text{baseline}} \times \gamma_{\text{temporal}} \times \gamma_{\text{Doppler}} \times \gamma_{\text{volume}} \times \gamma_{\text{thermal}} \times \gamma_{\text{processing}} \times \gamma_{\text{orbit}} \times \gamma_{\text{atmosphere}}. \quad (2)$$

Unwrapped phase is the continuous curve of the argument of the measured data and can be rigorously defined as an integral of arguments derivative, with the initial condition that the argument of the starting point is zero [16].

$$\arg[X(e^{j\omega})] = \int_0^\omega \arg'[X(e^{j\eta})] d\eta \quad \arg[X(e^{j0})] = 0, \quad (3)$$

where X is the complex signal, j is the imaginary number, ω is the argument, and η is the unit vector along the unwrapping path. Unwrapping can also be defined as the sum of the wrapped differences of the principal values [17,18]

$$\phi(m) = \phi(0) + \sum_{n=1}^m W_2 \Delta W_1 [\phi(n)], \quad (4)$$

where ϕ is the unwrapped phase, W is the wrapping operation, Δ denotes differentiation, m is the current pixel, and n is the summing variable. Both definitions are quite similar to one another, except for the initial phase in Eq. (3), the starting point value is set to zero. However, in Eq. (4), the reference point value is set to the signal's phase value.

Zebker and Goldstein [19] presented one of the first examples of high-resolution InSAR topography mapping with the unwrapped phase. Since then, there have been many unwrapping algorithms developed for the InSAR. (1) Goldstein's unwrapping algorithm was based on connecting nearest residues by branch cuts and unwrapping pixel-by-pixel without crossing the branch cuts [20]. Residues are defined as nonzero sums of phase values for pixels in a 2×2 neighborhood in a clockwise fashion. This can be represented with the curl of the phase gradient [20,21]

$$\begin{aligned} r(i, k) &= \nabla \times \nabla \phi(i, k) \\ &= W \delta_i \phi(i, k) + W \delta_k \phi(i + 1, k) - W \delta_i \phi(i, k + 1) \\ &\quad - W \delta_k \phi(i, k), \end{aligned} \quad (5)$$

where $r(i, k)$ is the residue for pixel (i, k) , $\nabla \times$ denotes curl, $\nabla \phi$ is the phase gradient, W is the wrapping operator, and δ_i is the gradient in the i direction. Results are unreliable with the nearest-neighbor branch-cut algorithm in areas with high residue density. In such areas, branch-cut placements are not straightforward. (2) An unwrapping algorithm based on cellular automaton, a cell-based discrete mathematical model in a gridded space, was developed for N -dimensional unwrapping [17]. In the cellular automaton algorithm, local inconsistencies in the 2×2 neighborhoods were masked out; however, branch cuts were not used to connect these inconsistencies. A lack of global residue mitigation limited the use of this algorithm. (3) A masking algorithm based on the second differences of the phase values was developed to eliminate the computationally expensive searching process for matching branch cuts [22]. The aim of these methods (1,2,3) is to alter the unwrapping path so that the unwrapping operation does not propagate errors. In some path-following unwrapping methods, the unwrapping function is optimized, instead of the unwrapping path. (4) The extended

Kalman filter [23–25] and (5) the particle filter [26] based unwrapping functions are examples of optimized unwrapping functions and are generally developed to unwrap along fixed-integration (sequential) paths. (6) Region-growth algorithms can be also considered path following, as region growing is done pixel-by-pixel [27].

Many non-path-following unwrapping algorithms were also developed. Some of these algorithms are: (7) weighted least squares using cosine transform [28], (8) multigrid weighted least squares unwrapping [29], (9) minimum network cost flow [30], (10) snaphu [31–33], and (11) Bayesian approach using *a priori* probability of the phase modeled as compound Gauss Markov random field [34]. Time-series generating algorithms, such as the permanent scatterer InSAR [35], small baselines interferometry [36], and Stanford Method for PS [37], can also be thought of as special cases of non-path-following unwrapping methods. Non-path-following algorithms are outside the scope of this paper.

For methods that unwrap interferograms pixel-by-pixel [20,22,24–27,38–41], unwrapping along an optimal path is important. However, less attention has been paid to path selection compared to unwrapping the algorithm itself. Here we specifically investigate path effects and present a new path algorithm that we believe is an improvement over existing methods.

3. Unwrapping Function

We compare the paths using the same unwrapping function, defined as

$$\hat{\phi}_0 = \sum_{k=1}^n \frac{\arg(\phi_0) + \arg(\phi_k \times \text{conj}(\phi_0))}{n}, \quad (6)$$

where $\hat{\phi}_0$ is the unwrapped value for the observed phase value (ϕ_0), and n indicates already unwrapped neighboring pixels. Equation (6) is a multidimensional modification of the phase tracking function [18]. Unwrapped neighbors are searched within the eight-cell neighborhood (Moore neighborhood) for two-dimensional applications [42]. For algorithms that provide a quality map, it is also possible to define a weighted version of Eq. (6):

$$\hat{\phi}_0 = \frac{\sum_{k=1}^n Q(k) \times [\arg(\phi_0) + \arg(\phi_k \times \text{conj}(\phi_0))]}{\sum_{k=1}^n Q(k)}, \quad (7)$$

where $Q(k)$ is the quality value for the neighboring pixels. The line scan (LS) algorithm does not offer a weighting function, and in order to have a fair comparison between all path algorithms, we base our analysis on Eq. (6). For comparison, the Envisat dataset was also processed using Eq. (7).

4. Unwrapping Paths

Unwrapping paths can be divided into two groups: (1) fixed integration (sequential), and (2) region grow-

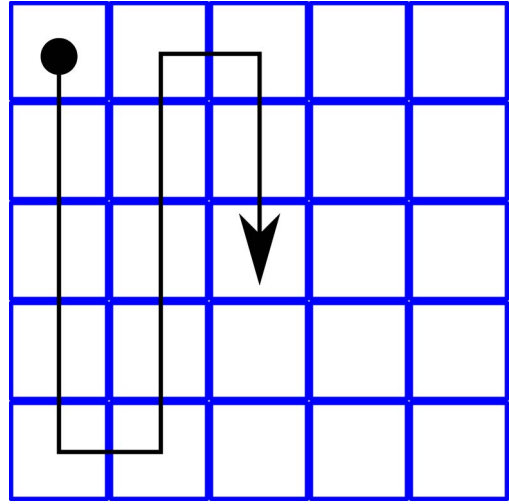


Fig. 1. (Color online) Example of a fixed-integration unwrapping path. The dot indicates the start of the path and the arrow indicates the direction. Path is shown as the black stroke. The path can be drawn from start to end without removing the tip of the pen.

ing. In a two-dimensional space, fixed-integration paths can be generated using space-filling curves (Peano curves [43–45]). An example of a commonly used space-filling curve is the LS path shown in Fig. 1.

While the aim of the unwrapping algorithms is to minimize the misfit, region-growing paths take a different approach, because misfit calculation require *a priori* knowledge of the solution as follows:

$$\chi^2 = \frac{1}{N} \times \sum_{k=0}^N \frac{[\hat{\phi}(k) - \phi(k)]^2}{\sigma^2(k)}, \quad (8)$$

where χ^2 is the misfit, $\hat{\phi}$ is the unwrapped phase, ϕ is the *a priori* phase, N is the number of total samples, and σ is the standard deviation, which is used to normalize the misfit [46]. Therefore, instead of minimizing the misfit, region-growing algorithms try to follow a quality function, minimizing a function F ,

$$F = \sum_{k=0}^N k * Q(k) \quad (9)$$

where k indicates the number of unwrapped pixels and $Q(k)$ represents the quality function, with high values indicating better quality and 0 indicating the lowest quality. N indicates the total number of pixels to be unwrapped. The unwrapping criterion requires visiting the pixels with higher quality first, in order to minimize the value of F . An example of a region-growing path is shown in Fig. 2. Unwrapping starts from the reference point, and continues with neighbors of already solved pixels, causing the unwrapping path to branch, unlike the continuous space-filling curve.

The reference point will define the initial conditions of the unwrapping path. Therefore, it is important to select a good starting point. All of the tested

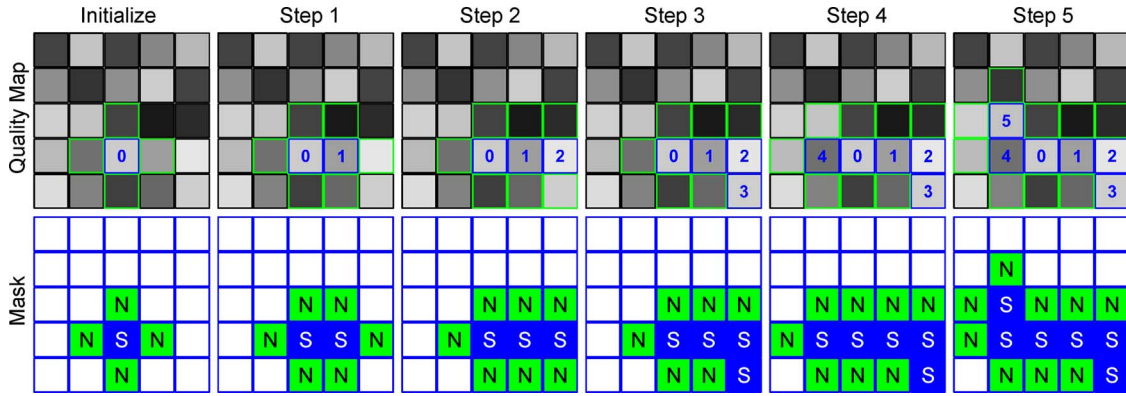


Fig. 2. (Color online) Example of a region-growth algorithm. In the top row, the gray-scale background indicates a measure of signal quality, where the lighter colors indicate higher quality. The bottom row shows the unwrapping mask, where solved points are marked with *S* and neighboring points are marked with *N*. During initialization, a reference point is selected. Pixels in the 4-pixel neighborhood are marked as ready to solve. Starting from the reference point, unwrapping continues with the highest quality neighbors.

paths with the exception of a LS can generate a quality map, which can be used to select a starting point. Even with a quality map, the selection of the optimal starting point may still be a difficult problem. The optimal starting point should minimize the misfit, which is available only after unwrapping is complete. In our tests, we used the upper-left corner (1,1) for all the synthetic interferograms. For the Envisat dataset, we define the starting point as the point with the highest coherence in the largest-continuous area with coherence over 0.4.

Six unwrapping paths are compared: (1) LS [25,26], (2) maximum coherence (MC), (3) phase derivative variance (PDV) [38], (4) phase derivative variance with branch-cut (PDV-BC) [20], (5) second-derivative reliability (SDR) [40,41], and (6) Fisher distance (FD). FD is the newly developed algorithm described here. Also, a benchmark is calculated following the minimum misfit path. Benchmark solution is only available when the solution is already known but useful for evaluating the quality of other algorithms.

A. Line Scan

LS is an example of the Peano curve and is a sequential unwrapping method. In this paper, it is implemented as a column-order continuous curve. Odd numbered columns are solved downwards, and even numbered columns are solved upwards (Fig. 1). Along this unwrapping path, four of eight neighbors in Eq. (6) are solved for pixels that are not on the edge of the interferogram. Although a high number of solved neighbors will cause the random noise to be averaged out, unwrapping errors due to aliasing and radar shadows propagate as a result of the fixed-integration path.

LS is used with special unwrapping functions in the literature such as extended Kalman filters and particle filters [25,26]. Filter-based unwrapping functions use previous information and certain assumptions to increase the robustness of the unwrapping operation. In this paper, we use a conventional unwrapping function, which does not employ special

assumptions about the data. Therefore, we limit the analysis of fixed-integration paths to LS and test it only for reference purposes.

B. Maximum Coherence

Coherency of the interferogram can be used as a quality map, where the pixels with higher coherence indicate high quality observations. Coherence of an interferogram is defined as [15]

$$\gamma = \frac{E[MS^*]}{\sqrt{E[MM^*]E[SS^*]}}, \quad (10)$$

where γ is coherence, E indicates expected value, the asterisk (*) denote complex conjugation, and M and S indicate master and slave acquisitions. The expected value needs to be estimated for each pixel, therefore, coherence can be estimated using

$$\hat{\gamma} = \frac{\frac{1}{N} \sum_{i=0}^N M_i S_i^*}{\sqrt{\frac{1}{N} \sum_{i=0}^N M_i M_i^* \frac{1}{N} \sum_{i=0}^N S_i S_i^*}}, \quad (11)$$

where $\hat{\gamma}$ denotes approximate coherence and N indicates the number of pixels in the neighborhood for coherence calculation. Throughout the paper, coherence is calculated over an area of $80 \text{ m} \times 80 \text{ m}$ corresponding to 4×20 pixels for the Envisat data. MC path starts from the reference point and follows the highest coherence available in the neighborhood of already solved pixels.

C. Phase Derivative Variance

The variance of the phase derivative is one of the earliest methods developed to define the unwrapping path [38,47]. The PDV is calculated over the four-cell neighborhood (von Neumann Neighborhood) and the pixel itself (total of five pixels). Calculated variances are then summed in all directions

$$\text{PDV}_k = \sum_{n=0}^N \sigma_x^2(n) + \sigma_y^2(n), \quad (12)$$

where PDV is calculated for a pixel k , using itself and four neighboring pixels indicated by N . For two-dimensional data, the PDVs are summed over two dimensions x and y . Our implementation of this algorithm and its branch-cut variation (PDV-BC) are based on Spottiswoode [48].

D. Phase Derivative Variance with Branch-Cut

Branch-cut algorithms use the fact that a unique unwrapped solution is only possible when the sum of wrapped phase values in any closed path equals zero [20]. Pixels where the sum of the wrapped phase values in any closed path does not equal zero are called residues. Each residue can have a positive or negative sign depending on the sum of the values. Branch cuts are placed to connect opposite signed residues to prevent the unwrapping path going through these non-zero-sum areas. Alternatively, residues can be connected to the border of the image. Since the branch cuts guarantee a unique unwrapping solution, the path algorithm is not important.

Correctly placed branch cuts make the unwrapping solution path independent or unique. There are several algorithms for placing branch cuts between residues, for example: nearest neighbor [20], minimum cost matching [49], stable marriages [50], modified nearest neighbor [51], phase field direction [52], and residue vector approach [53]. The phase field direction and residue vector approach are the only methods that use additional physical information.

In this paper, the PDV-BC path is constructed as follows: (1) find residues, (2) locate branch cuts, (3) mask out the branches, and (4) calculate the PDV path. When there are a small number of branch cuts, it is expected that the results from the PDV will be similar to the PDV-BC. Following the same approach, branch cuts can be implemented to improve results using any other path, but effects of branch cuts on different paths are beyond the scope of this paper.

E. Second-Derivative Reliability

SDR is based on the total change in horizontal, vertical, and diagonal directions of an eight-cell neighborhood (Moore neighborhood) [40,41]. Total change is then inverted to create a reliability map, where high values indicate more reliable pixels. Our implementation of this method follows Herraez *et al.* [40]. A possible shortcoming of this algorithm is its dependency on the second derivative of the data. Differentiation decreases the signal-to-noise (SNR) ratio [54], suggesting that the reliability values calculated by this approach can be problematic in low quality areas.

F. Fisher Distance

Like PDV, FD unwrapping path aims at extracting a quality map using the phase differences. Unlike

PDV, FD compares the phase differences to expected variance and gives importance to points with similarity in values in areas with lower variance. In general, lower variance points are located in the high quality areas. Fisher information is defined as the variance of the score in information theory. The score is defined as the gradient of the logarithm of the likelihood function [55–57]:

$$I(\phi) = E \left\{ \left[\frac{\partial}{\partial \phi} \log L(\phi; X) \right]^2 \middle| \phi \right\}, \quad (13)$$

where E is the expected value, L is the likelihood function of ϕ , which is also the probability density for ϕ ($L(\phi; X) = f(X, \phi)$, where f is the probability density). Fisher information, $I(\phi)$, can be thought as a metric of similarity at the given noise level. An example is a weather forecast of high daytime temperatures for a desert area in the summer. This would have a low Fisher information value, since most summer days in deserts have similarly high temperatures. On the contrary, the forecast of low daytime temperatures in a desert area in the summer would have a high Fisher information value. For other forecasts which would fall in between these two extreme scenarios, the Fisher information value would be calculated according to the forecasted daytime temperature and the expected variability of daytime temperatures at the given location for the given season.

If phase values for neighboring pixels are considered independent measurements, assuming a Gaussian probability density (likelihood) function, the Fisher information for neighboring pixel's can be calculated as

$$I_{0,1}(\phi) = \frac{(\phi_1 - \phi_0)^2}{2\sigma_0^2} + \log \sqrt{2\pi\sigma_0^2}, \quad (14)$$

where ϕ indicates the phase values, which are also the mean values defining the Gaussian distributions, σ is the standard deviation, and subscripts indicate current (0) and neighboring (1) pixels. Standard deviation of the phase values can be calculated from coherence values [58] or from PDV [38,47]. In certain cases, the Gaussian assumption does not hold [26,59], yet it is an assumption often made to simplify algorithm development [21,25,34,60–62]. Since the $I_{1,0}$ in Eq. (14) depends only on σ_0 without incorporating σ_1 , it is not symmetric (in the sense that the distance from pixel 0 to 1 is not the same as 1 to 0). Therefore, we use the average of both distances as a distance metric, defining FD as

$$I_{|01|} = 0.5 \times (I_{1,0} + I_{0,1}). \quad (15)$$

FD is a novel method developed for this study (at the time of writing the authors are unaware of any other phase unwrapping studies using Fisher information as a metric). In this paper, FD values for each

pixel are calculated over neighbors within the eight-cell (Moore) neighborhood. For standard deviation, we tested both the derived values from coherence [58] and the square-root of the PDV as described in Subsection 4.C. We obtained better results when the square-root of the PDV is employed, especially for the synthetic dataset. Results presented in this paper with the FD approach uses the PDV as σ_0^2 values in Eq. (14).

G. Benchmark

Unwrapping paths are compared to each other according to the misfit between the unwrapped solution ($\hat{\phi}$) and true phase (ϕ). The performance of the path can be estimated using Eq. (8). In general, the misfit (χ^2) will have larger values when the algorithm estimates a wrong solution early on, because the error will be propagated along the path. Standard deviation of the phase values (σ) are required to calculate the misfit. Standard deviation for the misfit is calculated using the coherence to standard deviation relation [58].

If the solution is already known, an unwrapping path can be defined to follow the minimum misfit. This can be used to define a reference (benchmark) solution to assess the performance of other algorithms. However, it must be noted that this path can only be defined when the true phase (ϕ) is already known, making it impossible to use in real-world applications.

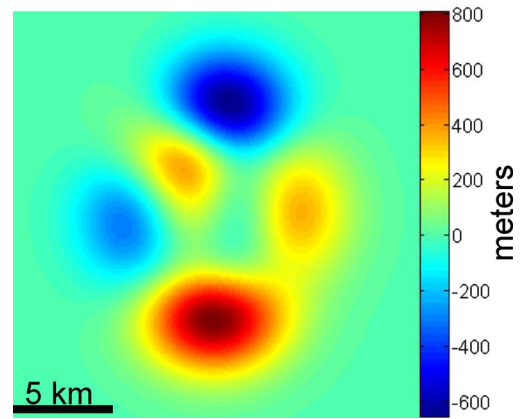


Fig. 3. (Color online) DEM generated for the synthetic dataset using Eq. (16). The dynamic range of the DEM is about 1450 m. The DEM is 256×256 pixels and each pixel has the dimensions $80 \text{ m} \times 80 \text{ m}$.

5. Test Datasets

The unwrapping paths described above are tested against synthetic datasets at four different perpendicular baselines, and three sets of real data, using Envisat interferograms.

A. Synthetic Dataset

The first dataset is based on a synthetic DEM generated using several shifted Gaussian functions to define a smooth surface with multiple local minima and local maxima [63]:

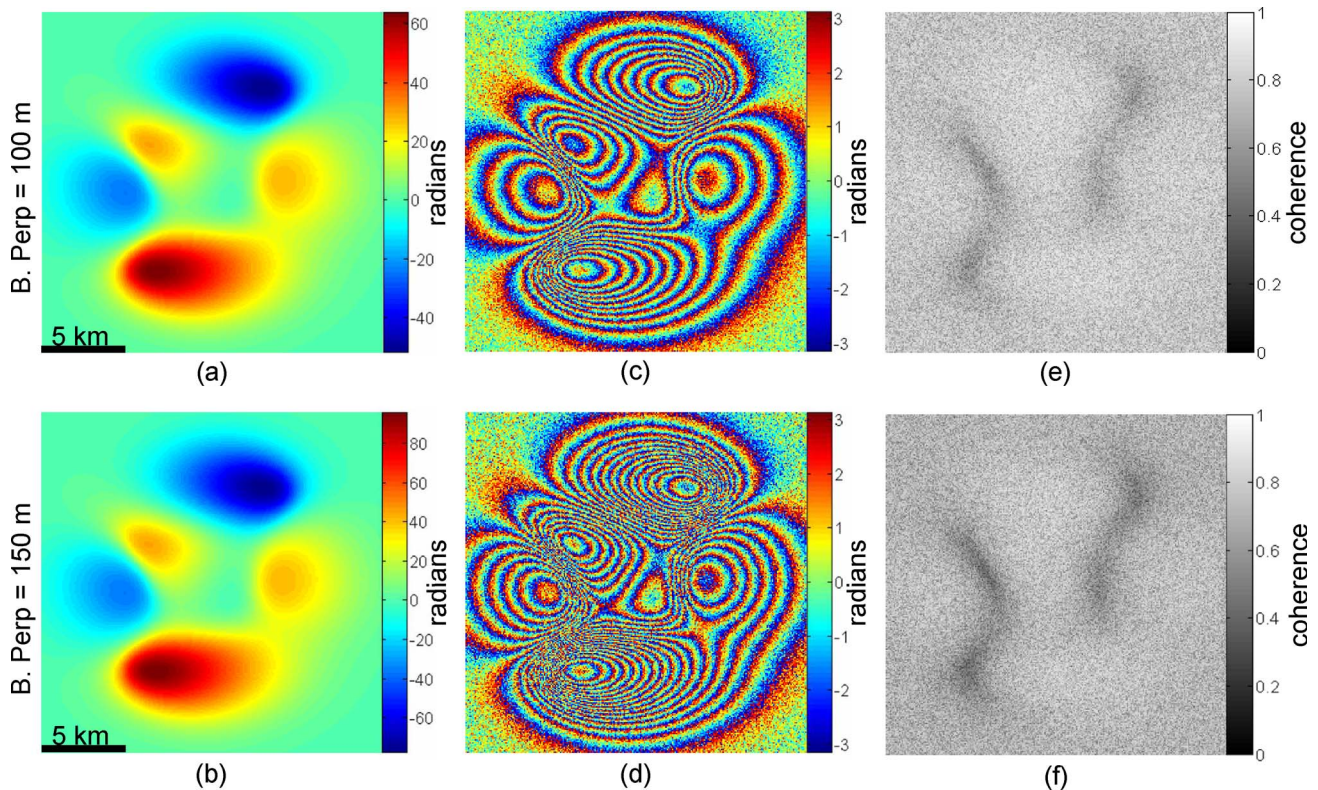


Fig. 4. (Color online) (a)–(b) The DEM phase, (c)–(d) interferogram phase, and (e)–(f) coherence are shown for 100 and 150 m baselines. The DEM phase shows the unwrapped, noise-free interferogram. Note the increased fringe rate in (d) compared to (c), as well as reduced coherence in (f) compared to (e).

Table 1. Baseline Information for the Envisat Interferograms

Master Slave (orbits)	Temporal Baseline (days)	Perpendicular Baseline (m)	Parallel Baseline (m)
14,337–14,838	35	−64.8	141.7
17,343–18,345	70	−37.3	246.0
18,345–19,347	70	44.4	−207.1

$$\begin{aligned} \text{DEM}(x,y) = & 3 \times (1-x)^2 \times e^{-x^2-(y+1)^2} \\ & - 10 \times (x/5 - x^3 - y^5) \times e^{-x^2-y^2} \\ & - 1/3 \times e^{-(x+1)^2-y^2}, \end{aligned} \quad (16)$$

where x and y indicate two-dimensional space, and e is the Euler number ($e = 2.7183$). The visualization of the resulting synthetic DEM is shown in Fig. 3.

An interferogram is simulated using the synthetic DEM (Fig. 3), with European Remote Sensing satellite-1 parameters [64]. Geometric coherence (γ_{baseline}) is calculated according to the slope of the radar-coded DEM and the perpendicular baseline. Additive random noise is calculated based on the geometric coherence values and total coherence (γ) is calculated as

$$\gamma = \gamma_{\text{baseline}} \times \gamma_{\text{noise}}. \quad (17)$$

Comparison of Eq. (17) with Eq. (3) shows that we are neglecting the effects of many other decorrelation factors in this dataset. Since the misfit calculation is based on the standard deviation, which is derived from coherence [58], the misfit values for this dataset will be higher than the second dataset where Envisat interferograms are used.

Figure 4 shows the DEM phase (unwrapped, radar-coded, noise-free phase), the interferogram (wrapped, with additive Gaussian noise), and coherence for 100 and 150 m perpendicular baseline cases. Although the perpendicular baseline difference is only 50 m between these datasets, due to the high gradients of the DEM the effects of aliasing increase. The overall coherence values also decrease about 0.1.

B. Envisat Dataset

This dataset uses Shuttle Radar Topography Mission (SRTM) 3 arc sec DEM and Envisat SAR data collected over Mexico City, Mexico. Baseline information is presented in Table 1. The topography covered by this scene has steep gradients. The small perpendicular baseline guarantees slow changing

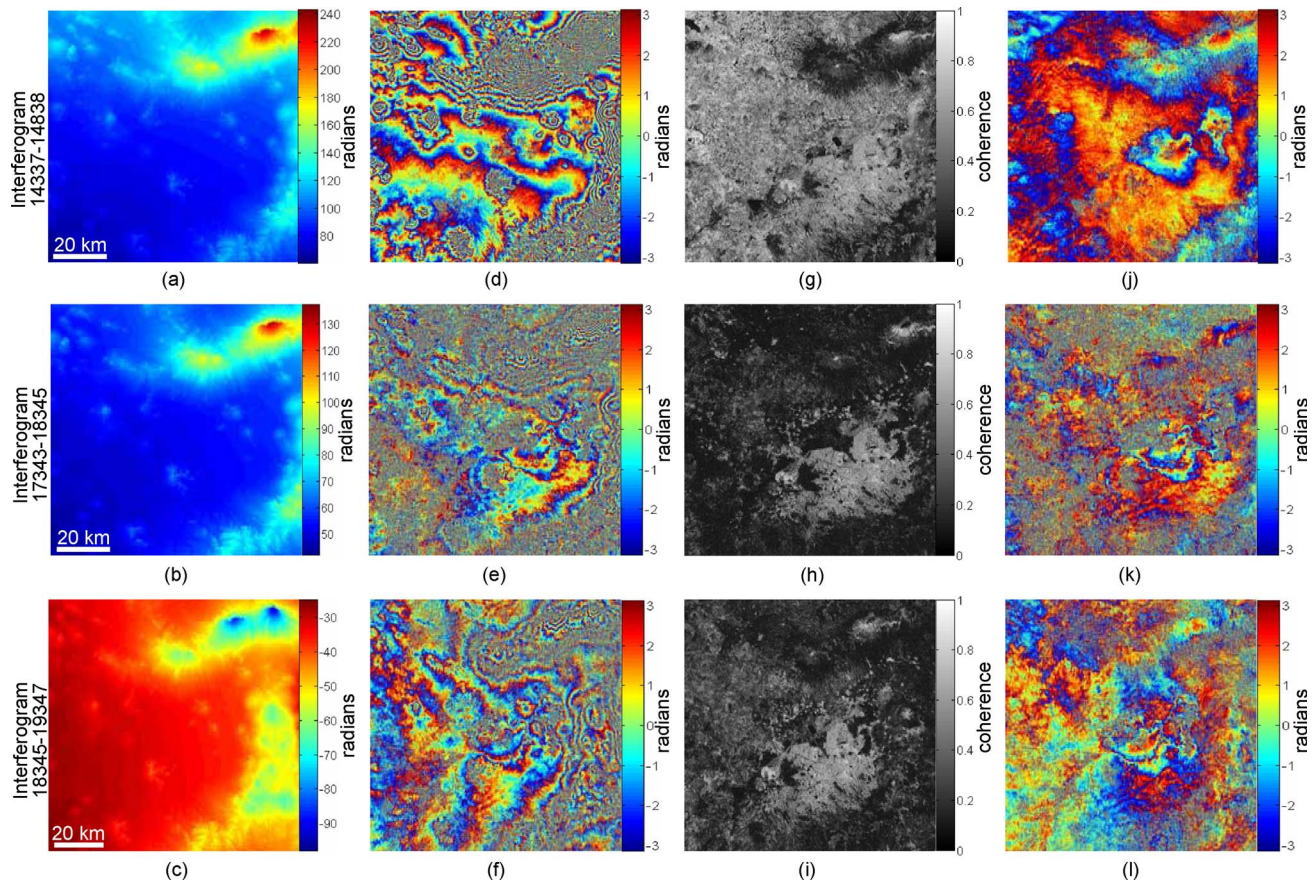


Fig. 5. (Color online) (a)–(c) The DEM phase, (d)–(f) interferogram phase, (g)–(i) coherence, and (j)–(l) residual phase for the Envisat interferograms 14,337–14,838, 17,343–18,345, and 18,345–19,347 over Mexico City. The DEM phase images are calculated using the SRTM DEM and baseline configurations from the interferograms. Note the reduced coherence in nonurban areas for interferograms 17,343–18,345, and 18,345–19,347 (h)–(i) compared to 14,337–14,838 (g). Also note the residuals are showing inconsistencies between the simulated DEM and interferogram phase (j)–(l).

Table 2. Misfit and Average Error for Synthetic Data

Method	$B\perp = 50\text{ m}$		$B\perp = 100\text{ m}$		$B\perp = 125\text{ m}$		$B\perp = 150\text{ m}$	
	$E[\chi^2]$	σ_{χ^2}	$E[\chi^2]$	σ_{χ^2}	$E[\chi^2]$	σ_{χ^2}	$E[\chi^2]$	σ_{χ^2}
LS	22.04	3.45	624.59	63.05	1085.24	102.36	1614.29	491.91
MC	0.98	0.01	3.12	0.69	32.46	21.70	926.40	467.49
PDV	1.10	0.07	19.85	7.64	70.34	14.48	532.73	370.07
PDV-BC	1.05	0.04	2.48	2.43	5.42	4.47	11.33	12.63
SDR	1.01	0.03	24.84	42.05	50.27	38.31	319.41	260.70
FD	1.03	0.03	8.17	1.49	27.29	4.72	78.57	12.06
Benchmark	1.02	0.02	1.13	0.02	1.21	0.01	1.30	0.02

^a $E[\chi^2]$ is average misfit, and σ_{χ^2} is standard deviation of misfit.

phase values over the low relief areas (inside Mexico City), and creates isolated steep phase slopes and aliasing in mountains. The interferograms are processed in a conventional way [65], and they are flattened but not filtered, in order not to introduce any artificial changes in the phase.

Mexico City has high subsidence rates in the urban area [7,66–68] which can introduce about 3.5 cm range change over the Envisat repeat cycle (35 days). Each fringe ($0 - 2\pi$) corresponds to 2.8 cm at the Envisat wavelength. The effects of subsidence are visible at the center of the residuals panels in Figs. 5(j)–5(l). The combined effect of the deformation and the limited resolution of the SRTM DEM cause residuals between the unwrapped DEM phase and interferogram, especially over the mountainous areas. These residuals will also cause the benchmark solution to deviate from the interferogram, making it challenging to evaluate algorithms.

6. Results

The results are shown in Tables 2 and 3 and Figs. 6 and 7. Misfit values are calculated for each test, as defined by Eq. (8). The *a priori* solution for the Envisat interferograms are not known; therefore, SRTM 3 arc sec DEM are used as the *a priori* solution in the misfit calculation.

A. Synthetic Dataset

Results for the synthetic interferograms are shown in Table 2, where misfit and its standard deviation are listed for each path. The values listed in Table 2 are averages of the same dataset over 10 runs with different additive random Gaussian noise. The aver-

age misfit ($E[\chi^2]$) represents the expected misfit for the method. The standard deviation (σ_{χ^2}) provides an estimate on the robustness of the algorithm, such that low standard deviations indicate robustness of the path algorithms to the changing random noise. For all the test cases, the LS algorithm has the largest average misfit and the largest standard deviation. The MC performs quite well for 50 and 100 m baselines, but errors increase dramatically with the increasing baseline. Larger baselines cause the geometric coherence (γ_{baseline}) to decrease indicating that the MC path is not useful when the overall coherence values are low. PDV and SDR obtain similar results for the 50 and 100 m baselines, though the SDR performs slightly better for the larger baselines. The PDV-BC reduces the misfit by almost 10 fold for the 100 m case, and about 50 fold for the 150 m case over the standard PDV. FD obtained low standard deviations for both cases and presents a similar performance to the PDV-BC. Benchmark results provide a lower limit for the misfit and the standard deviation. For the 50 m baseline case, all algorithms other than the LS obtain similar results to the benchmark.

The results for the synthetic dataset with 100 and 150 m perpendicular baseline are shown in Fig. 6. For both cases, problems with error propagation in the LS algorithm are visible. White areas in the branch-cut algorithm represent no-solution areas, which occur when branch cuts block access to parts of the interferogram. The MC, PDV, SDR, and FD algorithms show similar solutions, with errors visible to the left of the bottom extreme, and to the right of the upper extreme, coinciding with the areas masked out by the branch cut. The benchmark

Table 3. Misfits for the Envisat Dataset

Method	14,337–14,838		17,343–18,345		18,345–19,347	
	χ_U^2	χ_W^2	χ_U^2	χ_W^2	χ_U^2	χ_W^2
LS	92.14	N/A	72.77	N/A	71.10	N/A
MC	17.32	17.33	89.80	93.67	36.80	36.68
PDV	8.82	8.80	117.20	114.81	52.62	54.05
Branch Cut (PDV-BC)	37.73	38.94	32.54	32.52	16.26	16.26
SDR	14.84	15.09	137.35	138.60	91.62	84.51
FD	5.78	5.79	53.45	53.46	14.20	14.21
Benchmark	0.32	N/A	0.52	N/A	0.43	N/A

^a χ_U^2 obtained by the unweighted unwrapping function given in Eq. (6).

^b χ_W^2 obtained by the weighted unwrapping function given in Eq. (7)

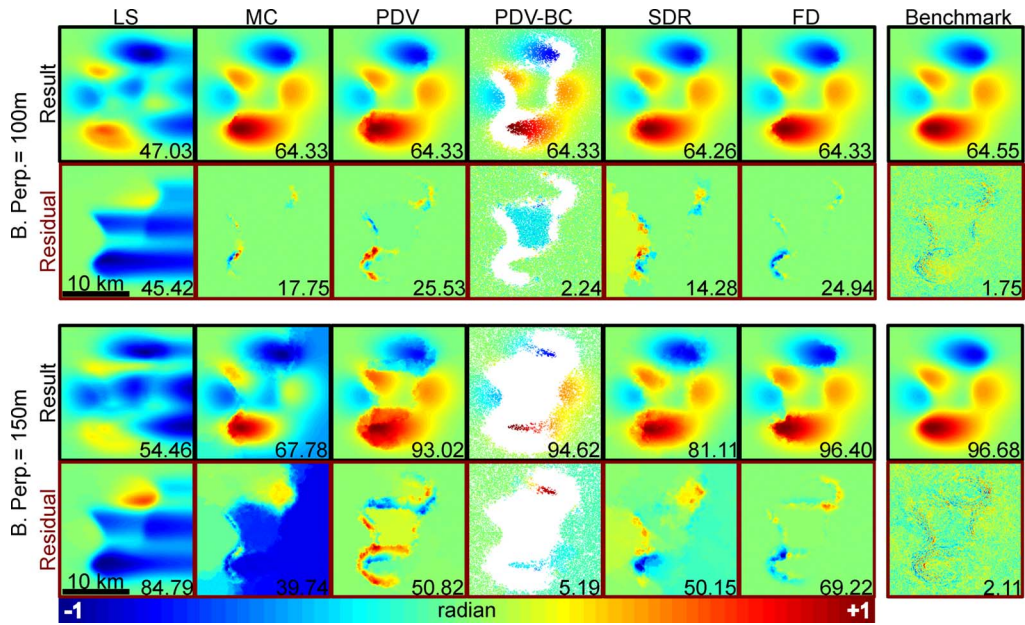


Fig. 6. (Color online) Average of ten solutions of synthetic dataset for 100 and 150 m perpendicular baselines with different Gaussian noise, for the compared paths. The scale is in radians and each figure is normalized with the number shown in the bottom right corner. The white areas in the PDV-BC solutions indicate inaccessible areas by branch cuts. Residual figures show the propagation of errors for each path. Note the small footprint of residuals for FD solutions.

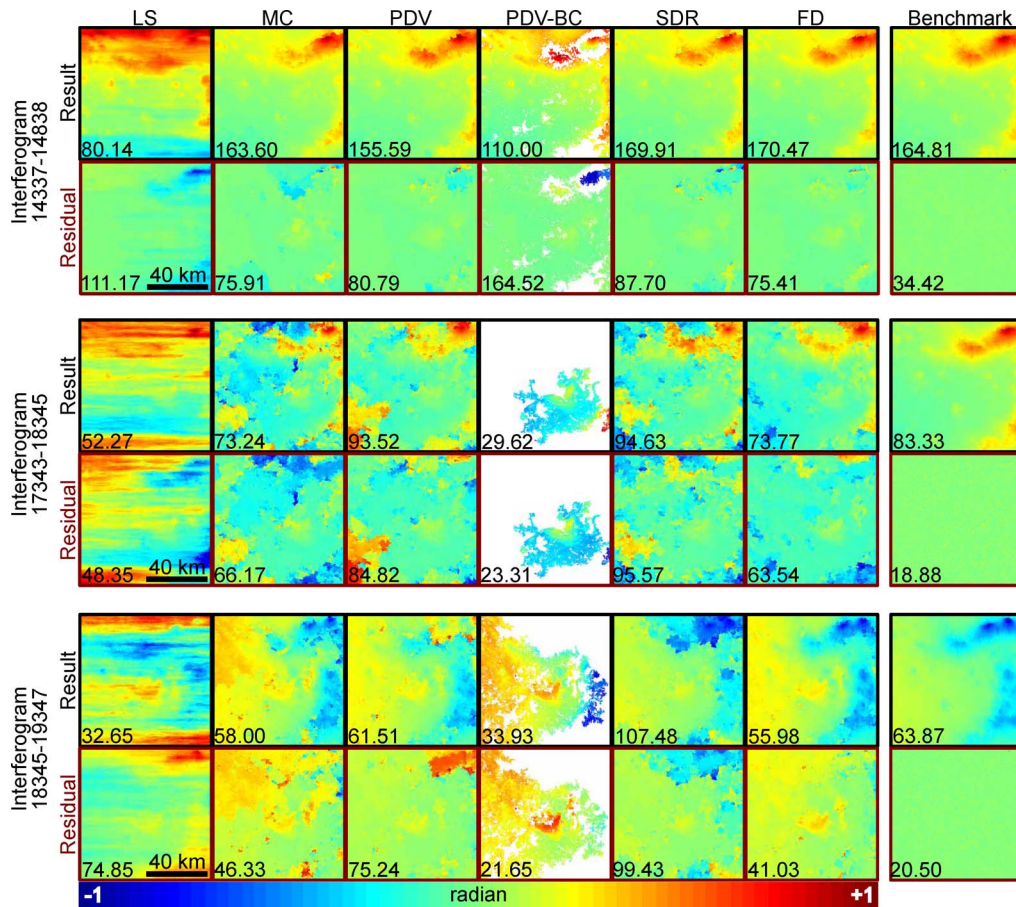


Fig. 7. (Color online) Solutions for the Envisat interferograms are shown in the same way as Fig. 6. Except the LS and PDV-BC, all paths return decent solutions for 14,337–14,838. Visual comparison of the results and residuals show that the FD returns reasonable results for interferograms 17,343–18,345 and 18,345–19,347 where others returned large residuals.

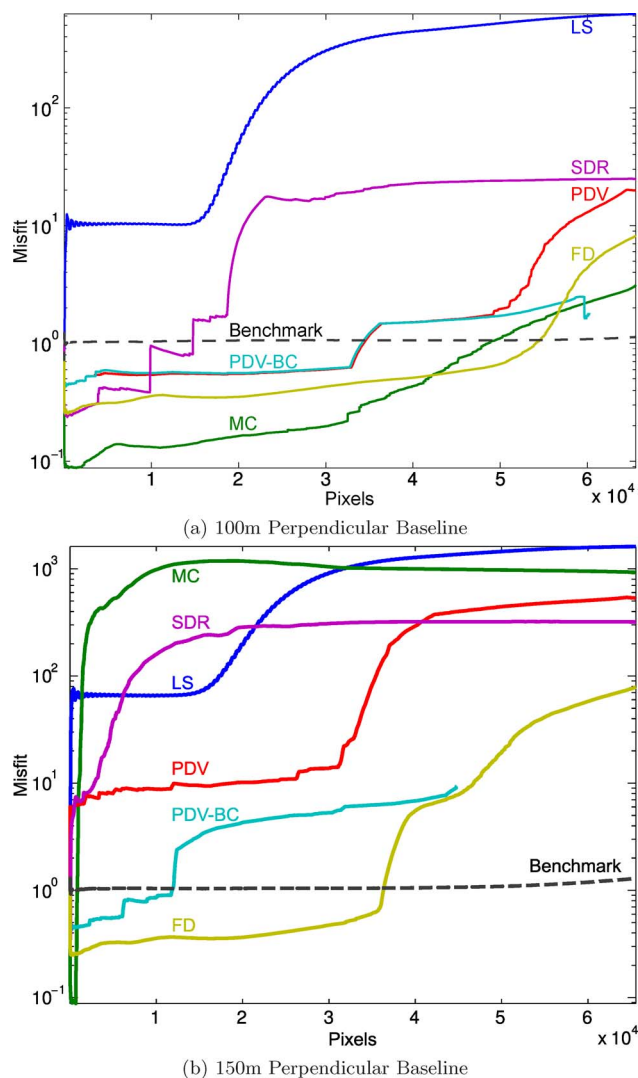


Fig. 8. (Color online) Misfit values along various unwrapping paths for synthetic interferograms with 100 and 150 m perpendicular baseline. The misfit (y axis) is in the log scale to better show the high range of values. The curvature of the misfit curves indicate how the algorithms perform along the path, such that rapid increase in misfit indicates propagated errors. (a) Note that the MC achieves very low misfit values. (b) Note that the MC starts propagating errors early on and does not recover. Also note that the FD starts propagating the errors the latest.

solution proves the existence of a path for an undeformed solution. For the 150 m baseline, all solutions look worse in comparison to the 100 m case. Errors are propagated further with the LS algorithm and the no-solution area is larger in the PDV-BC solution. Residuals for the FD are small for both cases, indicating that the FD algorithm does not propagate the errors as much as other algorithms. The MC spreads the errors even less for the 100 m baseline, suggesting that this algorithm performs well in high SNR areas.

B. Envisat Dataset

Misfits for Envisat interferograms are shown in Table 3. The Envisat interferograms are generated

using Envisat Advanced Synthetic Aperture Radar scenes and unlike the synthetic dataset, there is no additive random noise in the interferogram. Therefore, the interferograms in this dataset are only solved once. For the same reason the standard deviations cannot be calculated for this dataset. The Envisat dataset was unwrapped using both unweighted and weighted unwrapping functions as shown in Eqs. (6) and (7). The misfits calculated by both functions are similar, and hence the figures look identical in publication size, the figures for the weighted unwrapping results are not shown here. PDV and SDR obtained slightly better results for high-noise (17,343–18,345) and midnoise (18,345–19,347) interferograms. MC attained slightly worse misfits for the interferogram 17,343–18,345. Misfits reported in Table 3 for the LS algorithm are generally high; however, they are not the highest for all cases, as was the case for the synthetic dataset. This is due to the topography being solved at the end reducing the propagated error. MC obtains a low misfit for the 14,337–14,838 interferogram where the coherence values are generally high. The PDV and SDR algorithms perform well for the high coherence interferogram (14,337–14,838) but obtain large misfits for the other two interferograms. The FD and PDV-BC score the lowest two misfits for the interferograms 17,343–18,345 and 18,345–19,347. FD obtains the lowest misfit for 14,337–14,838.

The solutions can be seen in Fig. 7. Residuals are calculated using the SRTM DEM and are displayed in the second row of each group. Linear artifacts are visible in the LS results. For the 14,337–14,838 interferogram, the MC path result is similar to the benchmark solution; however, errors are propagated to the large portions of the interferogram for the other two cases. The PDV-BC path misinterprets the mountainous area for the 14,337–14,838 interferogram, and masks off the mountainous areas completely for the other two cases. MC, PDV, SDR, and FD obtain similar results for the high coherence interferogram (14,337–14,838). MC, PDV, and SDR propagates the error to the large areas for the interferograms 1,7343–18,345 and 18,345–19,347.

7. Discussion

While the results presented in this paper are obtained under the same conditions for each algorithm, the fact that the unwrapping function averages the solutions from neighboring cells can introduce a bias to our results. The bias is visible in Fig. 8, where some paths have lower misfit values compared to the benchmark. The unwrapping function introduces a bias toward the paths that have a slow, steady region growth.

All algorithms have higher misfits with higher noise levels. For the synthetic dataset (Table 2), the PDV-BC has the lowest misfit for all baselines. It must be noted that the PDV-BC algorithm implemented in this paper uses the same quality function as the PDV path. Therefore, when there are only a small number

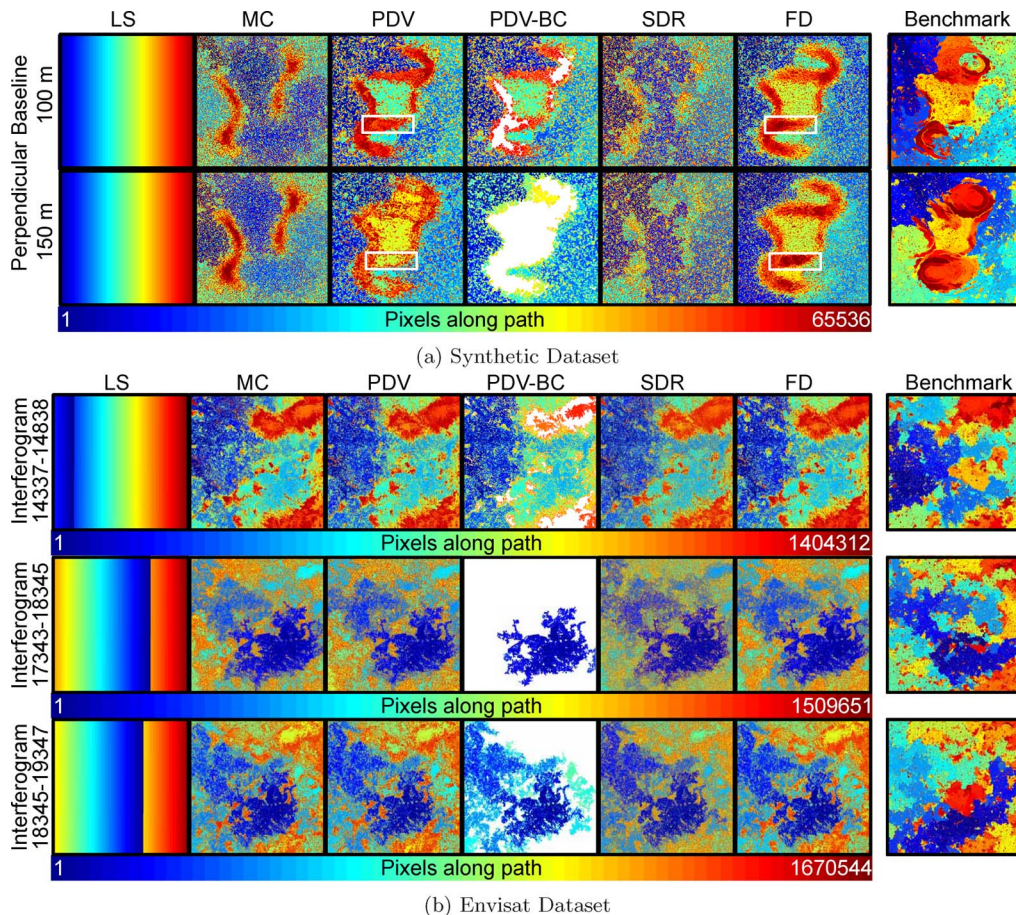


Fig. 9. (Color online) Paths followed by the path algorithms shown as a color-coded map. Blue indicates the beginning of the path and red indicates the end. (a) Note that the unreachable areas in the PDV-BC are larger with the 150 m baseline. Also note the differences between the PDV and FD paths. The PDV algorithm unwraps the areas shown in the white boxes earlier in the 150 m baseline case. The PDV-BC algorithm masks out those areas, and the FD algorithm delays the unwrapping of the areas marked with the white boxes until the end. (b) Note that the paths are quite different for the MC, PDV, PDV-BC, SDR and FD algorithms for different interferograms. This is due to the differences in general coherence level of the interferograms. The LS path changes depending on the different starting points for each interferogram.

of branch cuts, the PDV and PDV-BC algorithms return similar misfits, as shown in the 50 and 100 m case.

Residuals in Fig. 6 indicate where the errors are located. The LS algorithm creates a smearing effect, propagating the error to a large portion of the image. The MC path has the biggest difference between 100 and 150 m solutions. MC provides the smallest area of errors in the 100 m case; however, in the 150 m case, its results are almost as bad as the LS. PDV spreads the error in the center of the image, more pronounced in the residuals for the 150 m case. SDR solves for the center of the interferogram correctly; however, it spreads the errors to the left and right of the image. Branch cut masks out the problematic areas successfully in the 100 m case, but in the 150 m case it returns large residuals around the top extreme. FD prevents the errors from spreading quite well in both cases, and high residuals cover small areas in comparison to other methods.

Analyzing how misfit changes along the unwrap-path can give us some idea of where the errors

occur. An optimal unwrapping algorithm should not create any large misfits in the beginning of the path, accumulating the bad points to the end. Having the bad pixels at the end of the path can give the user a chance to mask out those areas easily, as well as reducing the error propagation. The slope of the curves shown in Fig. 8 indicate the performance of the path at that point. If the slope is positive, it means that the path is spreading errors, whereas a negative slope indicates correct solutions reducing the average misfit. The misfit values shown in these curves are averaged like the values in Table 2. Benchmark values are almost constant along its path, indicating that the path does not have any problem areas. The sharp rises in misfit values are an indication of large errors. The FD path has the latest rise of misfit values in both figures, indicating it solved the bad points at the end of the path. PDV and PDV-BC have similar misfit curves in the 100 m case [Fig. 8(a)], but differ in the 150 m case [Fig. 8(b)]. Differences between the PDV and PDV-BC curves show the effect of branch cuts. LS and SDR have

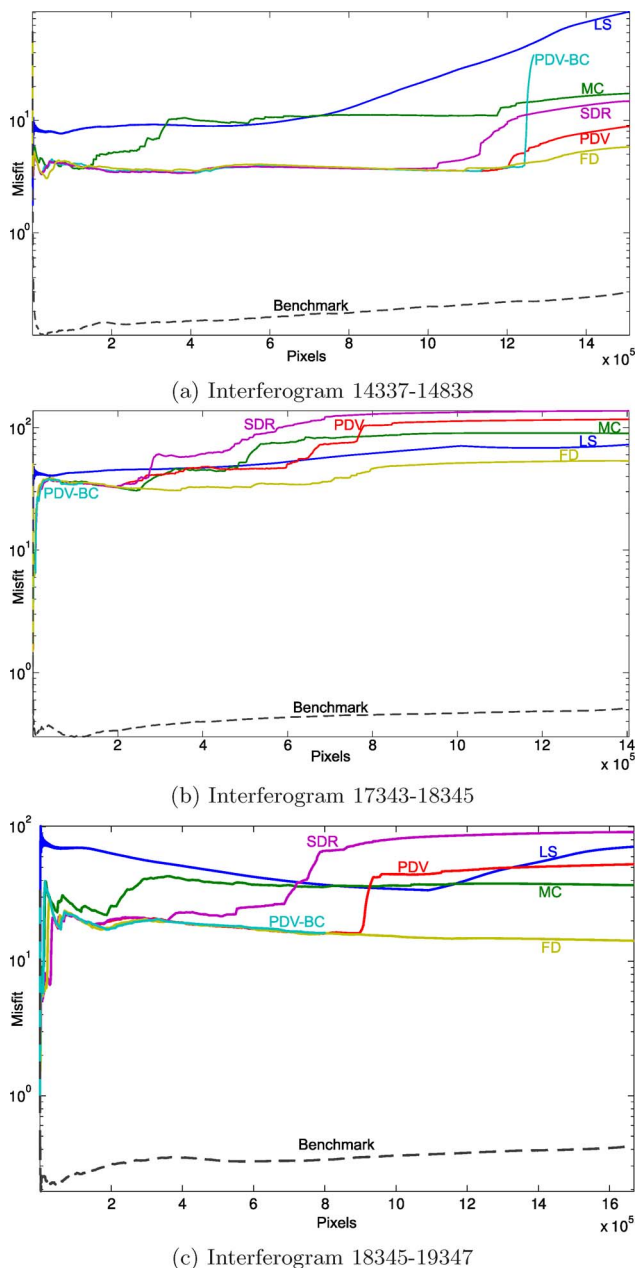


Fig. 10. (Color online) Misfit values along various unwrapping paths for the Envisat interferograms. The misfit (y axis) is shown in log scale to better represent the high range of values. (a) Note the last rise in the PDV-BC path. This indicates that the PDV-BC successfully left a bad area until the end, and the unwrapping function failed to unwrap that area. The PDV, PDV-BC, SDR and FD have similar misfits, indicating similar paths, with differences at the end. (b) The PDV-BC path ends early on. The LS performs better than the MC, PDV, and SDR. (c) The MC achieves better misfit than the LS, PDV, and SDR. The PDV, PDV-BC, and FD start the same. The FD achieves the lowest misfit.

early sharp rises, propagating errors to the large areas. The stepping appearance of the SDR misfits in the 100 m case [Fig. 8(a)] indicates that the path visits bad areas one after the other and cannot recover.

Figure 9 show the paths taken by each algorithm. For the synthetic dataset [Fig. 9(a)], the LS path is

the same for both cases by definition. The MC, PDV, PDV-BC, SDR, and FD paths have minor differences. The benchmark path has some differences between 100 and 150 m: (1) the solution of the top and bottom extremes are delayed, and (2) the boundaries of the central area are delayed. The delayed areas in MC, PDV, and FD are easily noticeable (orange to red colors). The SDR paths, do not have distinct areas that are delayed, and the path image has a grainier look.

The Envisat dataset consists of three interferograms with short baselines providing smooth phase gradients in the flats, and some aliasing over the mountains. paths are shown in Fig. 9(b). Residuals for interferogram 14,337–14,838 in Fig. 7 show that MC, PDV, and SDR have low misfit in general, especially in mountainous areas. On the contrary, they have high residuals for the interferograms 17,343–18,345 and 18,345–19,347. The paths for MC, PDV, SDR, and FD look similar in a general sense for all interferograms in Fig. 9(b). One difference is that the mountainous area on the top-right corner is delayed more in FD and MC in comparison to PDV and SDR. This delay is more obvious for interferograms 17,343–18,345 and 18,345–19,347, where the blue-green colors are surrounded by the orange to red in the top-right corner.

Figure 9(b) shows that all quality map driven algorithms solved the gentle sloping areas first for the Envisat dataset. The paths of the PDV, PDV-BC, SDR, and FD look rather similar, explaining the similar performances shown in Fig. 10(a). The sloping behavior of the benchmark misfit curve is due to the residuals shown in Figs. 5(j)–5(l). For this test case (14,337–14,838), the PDV-BC scores are worse than the PDV algorithm, possibly due to incorrectly placed branch cuts.

For the 17,343–18,345 interferogram, the misfit curves are given in Fig. 10(b). All paths attain large misfit values early on the unwrapping path, indicating poor quality of the interferogram. The LS, MC, PDV, and SDR score similar values. The PDV-BC scores the lowest misfit; however, it only unwraps the highest quality parts of the interferogram, leaving a large area masked out. The FD obtains the lowest misfit omitting the PDV-BC. It is important to note that even though the LS is not a quality driven algorithm, it achieved better results than the MC, PDV and SDR, because the starting point and the distribution of mountainous areas prevented propagation of error to large areas.

The quality of the interferogram 18,345–19,347 is between 14,337 and 14,838 and 17,343 and 18,345. Therefore the expected misfit values should be between 14,337 and 14,838 and 17,343–18,345 for all algorithms (Table 3). This is the case for all algorithms, except the PDV-BC, where the misfit for 17,343–18,345 is lower than the 14,337–14,838 due to early termination. The misfit curves are shown in Fig. 10(c). The PDV, PDV-BC, and FD started off the same. The PDV-BC path ended before the PDV misfit started to rise, indicating that the

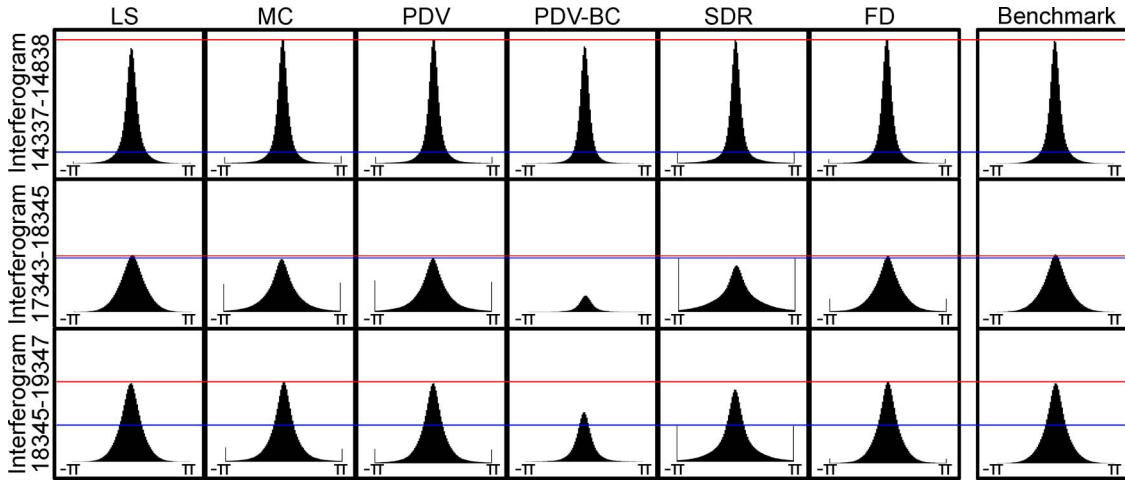


Fig. 11. (Color online) Histograms show the combined phase derivative errors in both directions (azimuth and range) for each unwrapping path. The y range of all the plots are between 0 and 250,000, whereas the x range is between $-\pi$ and π . Red and blue guidelines are drawn to aid comparison. The red line marks the highest peak in the histograms, and the blue line indicates the highest peak of cycle error.

masked off area had bad quality. The FD path solves that area, without having any trouble and lowering the misfit all along with a gentle negative slope. The LS starts off with a large misfit, as it hits the top mountainous area in the beginning of the path going toward the top left corner from the starting point. It lowers the misfit until the second portion where the path goes from the starting point to the lower-right corner through the mountainous area on the right. The SDR misfits keep rising and ends up with the largest misfit among tested paths.

The comparison of weighted and unweighted unwrapping functions showed that the performances of both functions were similar when coupled with the respective quality maps for MC, PDV, PDV-BC, SDR, and FD. While PDV and SDR obtained slightly better results for interferograms 17,343–18,345 and 18,345–19,347, respectively, the MC misfit was worse with the weighted unwrapping function. This can be due to the fact that coherence is over estimated in areas of low coherence using the maximum likelihood estimator given in Eq. (11) (i.e., $\hat{\gamma} \geq \gamma$) [21]. This is also in line with the low misfits obtained by MC in a high quality interferogram (14337–14838), whereas the other interferograms with a lower SNR resulted in high misfits using MC.

In this study, six path algorithms are compared using synthetic and Envisat SAR data, using a single unwrapping function. It is possible that use of a certain dataset with a particular unwrapping function could deviate from the results obtained in this paper. However, the generality of the analysis can be addressed based on Friis' formula from the telecommunication's theory [69]:

$$F = F_1 + \frac{F_2 - 1}{G_1} + \frac{F_3 - 1}{G_1 G_2} + \cdots + \frac{F_K - 1}{G_1 G_2 \cdots G_{K-1}}, \quad (18)$$

where F indicates the overall system noise figure, F_K is the noise figure, and G_K is the gain associated with the K^{th} subsystem. Under the Gaussian assumption,

the noise figure related to the unwrapping of the K^{th} pixel along a path, for the nonweighted unwrapping function can be defined as

$$F_K = \frac{\text{SNR}_{\text{IN}}}{\text{SNR}_{\text{OUT}}} \approx \sqrt{N}, \quad (19)$$

where SNR stands for signal-to-noise ratio, IN and OUT represent the input and output of the unwrapping function for pixel K , and N is the number of neighbors. As shown in Eq. (19), the input to output SNR values are proportional to number of neighbors, because the expected variance of the unwrapped pixel decreases with the number of independent observations (i.e., equations) defined by the already unwrapped neighboring pixels [70,71]. Equation (18) underlines the importance of unwrapping high quality pixels due to error propagation along the unwrapping path. Equation (19) shows the importance of delaying the low quality pixels, as the gain of the unwrapping function will increase with the number of independent equations related to the unwrapped neighbors. In other words, delaying the bad quality pixels not only delays the propagated error, but also increases the quality of the result. Combining Eqs. (18) and (19) indicates the importance of the path and the generality of the results presented in this paper.

Following the Friis' formula, a path-following unwrapping system can be divided into two parts: (1) individual unwrapping operations, and (2) the order of operations. The misfit figures reported in Tables 2 and 3 indicate the performances of the complete system. The effect of the order of operations on the misfit is analyzed using different paths, namely, the LS, MC, PDV, SDR, FD. It is also possible to look at the effect of the order of operations to the individual unwrapping operations. The errors for individual unwrapping operations can be analyzed looking at the error on the phase derivative. Because

the same unwrapping function is used for all algorithms, differences in the results are due to delaying the low quality pixels, as chosen by each path. The histograms in Fig. 11 are scaled to the same height, providing an easy comparison of phase derivative errors. If there were no errors, the histogram would have no tails and a very large peak at the center (zero); therefore, the height of the center peak provides visual information on how successful the unwrapping operations were. Cycle errors (errors larger than $\pm\pi$) and the width of the histograms indicate how poorly the unwrapping function performed. We see that the LS and PDV-BC algorithms produce minimal cycle errors. For all cases, the SDR algorithm results in the largest cycle errors. The fact that the LS algorithm does not generate large cycle errors indicates that the unwrapping operations are done successfully. However, the bad integration path caused the total misfit to rise. As seen from the results in Fig. 11, the FD algorithm provides a high center peak with small cycle errors.

8. Conclusion

We tested six unwrapping paths with two different datasets. The first dataset focused on the effects of geometric decorrelation, creating a synthetic interferogram for different perpendicular baselines. The second dataset utilized three Envisat interferograms with small baselines at different qualities. Among the tested algorithms, the FD algorithms performed well, scoring either the best or second-best misfit values in all tests. Correct placement of branch cuts improve the results for the PDV path, and possibly any others, but may create large areas masked out in low quality interferograms. It is important to note that tested paths might get different results if the unwrapping function is replaced with another one. Therefore, even though we believe that the FD path should improve results with any unwrapping function, this remains to be tested in the future. However, for the limited cases tested, our new path selection algorithm, based on the Fisher information theory, appears to achieve better results.

The first author would like to thank the National Aeronautics and Space Administration (NASA) for the NASA Earth and Space Science Fellowship provided between 2007-2010, 09-Earth-09R-61. We thank the European Space Agency for providing the Envisat Advanced Synthetic Aperture Radar images through the Category 1 project 1409 to Enrique Cabral-Cano. We also thank anonymous reviewers for their insightful and constructive comments.

References

1. H. A. Zebker and P. Rosen, "On the derivation of coseismic displacement fields using differential radar interferometry: the Landers earthquake," in *Geoscience and Remote Sensing Symposium, 1994. IGARSS '94. Surface and Atmospheric Remote Sensing: Technologies, Data Analysis and Interpretation, International*, vol. 1, (IEEE, 1994), pp. 286-288.
2. M. Simons, Y. Fialko, and L. Rivera, "Coseismic deformation from the 1999 Mw 7.1 Hector Mine, California, earthquake as inferred from InSAR and GPS observations," *Bull. Seismol. Soc. Am.* **92**, 1390-1402 (2002).
3. R. Bürgmann, M. Ayhan, E. Fielding, T. Wright, S. McClusky, B. Aktug, C. Demir, O. Lenk, and A. Turkezer, "Deformation during the 12 November 1999 Duzce, Turkey, earthquake, from GPS and InSAR data," *Bull. Seismol. Soc. Am.* **92**, 161-171 (2002).
4. R. Lanari, P. Lundgren, and E. Sansosti, "Dynamic deformation of Etna volcano observed by satellite radar interferometry," *Geophys. Res. Lett.* **25**, 1541-1544 (1998).
5. T. Wright, C. Ebinger, J. Biggs, A. Ayele, G. Yirgu, D. Keir, and A. Stork, "Magma-maintained rift segmentation at continental rupture in the 2005 Afar dyking episode," *Nature* **442**, 291-294 (2006).
6. F. Amelung, D. L. Galloway, J. W. Bell, H. A. Zebker, and R. J. Lacznaiak, "Sensing the ups and downs of Las Vegas: InSAR reveals structural control of land subsidence and aquifer-system deformation," *Geology* **27**, 483-486 (1999).
7. G. Bawden, W. Thatcher, R. Stein, K. Hudnut, and G. Peltzer, "Tectonic contraction across Los Angeles after removal of groundwater pumping effects," *Nature* **412**, 812-815 (2001).
8. Z. Perski, "Applicability of ERS-1 and ERS-2 InSAR for land subsidence monitoring in the Silesian coal mining region, Poland," *International Archives of Photogrammetry and Remote Sensing* **32**, 555-558 (1998).
9. N. Gourmelen, F. Amelung, F. Casu, M. Manzo, and R. Lanari, "Mining-related ground deformation in Crescent Valley, Nevada: implications for sparse GPS networks," *Geophys. Res. Lett.* **34**, L09309 (2007).
10. R. M. Goldstein, H. Engelhardt, B. Kamb, and R. M. Frolich, "Satellite radar interferometry for monitoring ice sheet motion—application to an Antarctic ice stream," *Science* **262**, 1525-1530 (1993).
11. S. Wdowinski, F. Amelung, F. Miralles-Wilhelm, T. Dixon, and R. Carande, "Space-based measurements of sheet-flow characteristics in the Everglades wetland, Florida," *Geophys. Res. Lett.* **31**, L15503 (2004).
12. S. Wdowinski, S.-W. Kim, F. Amelung, T. Dixon, F. Miralles-Wilhelm, and R. Sonenshein, "Space-based detection of wetlands surface water level changes from L-band SAR interferometry," *Rem. Sens. Environ.* **112**, 681-696 (2008).
13. M. I. Skolnik, *Introduction to Radar Systems*, 2nd ed. (McGraw Hill, 1980).
14. R. F. Hanssen, *Radar Interferometry: Data Interpretation and Error Analysis* (Kluwer, 2001).
15. H. A. Zebker and J. Villasenor, "Decorrelation in interferometric radar echoes," *IEEE Trans. Geosci. Remote Sens.* **30**, 950-959 (1992).
16. J. Tribolet, "A new phase unwrapping algorithm," *IEEE Trans. Acoust. Speech Signal Process.* **25**, 170-177 (1977).
17. D. C. Ghiglia, G. A. Mastin, and L. A. Romero, "Cellular-automata method for phase unwrapping," *J. Opt. Soc. Am. A* **4**, 267-280 (1987).
18. K. Itoh, "Analysis of the phase unwrapping algorithm," *Appl. Opt.* **21**, 2470-2470 (1982).
19. H. A. Zebker and R. M. Goldstein, "Topographic mapping from interferometric synthetic aperture radar observations," *J. Geophys. Res.* **91**, 4993-4999 (1986).
20. R. M. Goldstein, H. A. Zebker, and C. L. Werner, "Satellite radar interferometry: two-dimensional phase unwrapping," *Radio Sci.* **23**, 713-720 (1988).
21. R. Bamler and P. Hartl, "Synthetic aperture radar interferometry," *Inverse Probl.* **14**, R1-R54 (1998).
22. D. J. Bone, "Fourier fringe analysis: the two-dimensional phase unwrapping problem," *Appl. Opt.* **30**, 3627-3632 (1991).

23. J. M. N. Leitaó and M. A. T. Figueiredo, "Absolute phase image reconstruction: a stochastic nonlinear filtering approach," *IEEE Trans. Image Process.* **7**, 868–882 (1998).
24. M. Kim and H. Griffiths, "Phase unwrapping of multibaseline interferometry using Kalman filtering," presented at the 7th International Conference on Image Processing and its Applications, Manchester, UK (13–15 July 1999).
25. O. Loffeld, H. Nies, S. Knedlik, and Y. Wang, "Phase unwrapping for SAR interferometry: a data fusion approach by Kalman filtering," *IEEE Trans. Geosci. Remote Sens.* **46**, 47–58 (2008).
26. J. Martinez-Espla, T. Martinez-Marin, and J. Lopez-Sanchez, "A particle filter approach for InSAR phase filtering and unwrapping," *IEEE Trans. Geosci. Remote Sens.* **47**, 1197–1211 (2009).
27. W. Xu and I. Cumming, "A region-growing algorithm for InSAR phase unwrapping," *IEEE Trans. Geosci. Remote Sens.* **37**, 124–134 (1999).
28. D. C. Ghiglia and L. A. Romero, "Robust two-dimensional weighted and unweighted phase unwrapping that uses fast transforms and iterative methods," *J. Opt. Soc. Am. A* **11**, 107–117 (1994).
29. M. Pritt, "Phase unwrapping by means of multigrid techniques for interferometric SAR," *IEEE Trans. Geosci. Remote Sens.* **34**, 728–738 (1996).
30. M. Costantini, "A novel phase unwrapping method based on network programming," *IEEE Trans. Geosci. Remote Sens.* **36**, 813–821 (1998).
31. C. W. Chen and H. A. Zebker, "Network approaches to two-dimensional phase unwrapping: intractability and two new algorithms," *J. Opt. Soc. Am. A* **17**, 401–414 (2000).
32. C. W. Chen and H. A. Zebker, "Two-dimensional phase unwrapping with use of statistical models for cost functions in nonlinear optimization," *J. Opt. Soc. Am. A* **18**, 338–351 (2001).
33. C. W. Chen and H. A. Zebker, "Phase unwrapping for large SAR interferograms: statistical segmentation and generalized network models," *IEEE Trans. Geosci. Remote Sens.* **40**, 1709–1719 (2002).
34. J. M. Bioucas-Dias and J. Leitaó, "InSAR phase unwrapping: a Bayesian approach," in *Geoscience and Remote Sensing Symposium, 2001* (IEEE, 2001), pp. 396–400.
35. A. Ferretti, C. Prati, and F. Rocca, "Permanent scatterers in SAR interferometry," *IEEE Trans. Geosci. Remote Sens.* **39**, 8–20 (2001).
36. P. Berardino, G. Fornaro, R. Lanari, and E. Sansosti, "A new algorithm for surface deformation monitoring based on small baseline differential SAR interferograms," *IEEE Trans. Geosci. Remote Sens.* **40**, 2375–2383 (2002).
37. A. Hooper, "Persistent scatter radar interferometry for crustal deformation studies and modeling of volcanic deformation," Ph.D. dissertation (Stanford University, 2006).
38. D. C. Ghiglia and M. D. Pritt, *Two-Dimensional Phase Unwrapping: Theory, Algorithms and Software* (Wiley, 1998).
39. R. Krämer, "Auf Kalman-Filtern basierende Phasen- und Parameterestimation zur Lösung der Phasenvieldeutigkeitproblematik bei der Höhenmodellerstellung aus SAR-Interferogrammen," Ph.D. dissertation (Universität-GH Siegen, 1998).
40. M. Herráez, D. Burton, M. Lalor, and M. Gdeisat, "Fast two-dimensional phase-unwrapping algorithm based on sorting by reliability following a noncontinuous path," *Appl. Opt.* **41**, 7437–7444 (2002).
41. H. Abdul-Rahman, M. Gdeisat, D. Burton, M. Lalor, F. Lilley, and C. Moore, "Fast and robust three-dimensional best path phase unwrapping algorithm," *Appl. Opt.* **46**, 6623–6635 (2007).
42. E. Moore, "Machine models of self-reproduction," in *Mathematical Problems in the Biological Sciences*, R. Bellman, ed. (American Mathematical Society, 1962), pp. 17–33.
43. G. Peano, "On a curve which entirely fills a plane domain," *Math. Ann.* **36**–157160 (1890).
44. H. Sagan and J. Holbrook, *Space-Filling Curves* (Springer-Verlag, 1994).
45. C. A. Pickover, *The Math Book* (Sterling, 2009).
46. W. Press, S. Teukolsky, W. Vetterling, and B. Flannery, *Numerical Recipes in C* (Cambridge University, 1992).
47. B. R. Hunt, "Matrix formulation of the reconstruction of phase values from phase differences," *J. Opt. Soc. Am.* **69**, 393–399 (1979).
48. B. Spottiswoode, "2D phase unwrapping algorithms," <http://www.mathworks.com/matlabcentral/fileexchange/22504>.
49. J. Buckland, J. Huntley, and S. Turner, "Unwrapping noisy phase maps by use of a minimum-cost-matching algorithm," *Appl. Opt.* **34**, 5100–5108 (1995).
50. J. Quiroga, A. González-Cano, and E. Bernabeu, "Stable-marriages algorithm for preprocessing phase maps with discontinuity sources," *Appl. Opt.* **34**, 5029–5038 (1995).
51. R. Cusack, J. M. Huntley, and H. T. Goldrein, "Improved noise-immune phase-unwrapping algorithm," *Appl. Opt.* **34**, 781–789 (1995).
52. B. Gutmann and H. Weber, "Phase unwrapping with the branch-cut method: role of phase-field direction," *Appl. Opt.* **39**, 4802–4816 (2000).
53. S. Karout, M. Gdeisat, D. Burton, and M. Lalor, "Residue vector, an approach to branch-cut placement in phase unwrapping: theoretical study," *Appl. Opt.* **46**, 4712–4727 (2007).
54. R. Pawula, S. Rice, and J. Roberts, "Distribution of the phase angle between two vectors perturbed by Gaussian noise," *IEEE Trans. Commun.* **30**, 1828–1841 (1982).
55. F. Edgeworth, "On the probable errors of frequency-constants (contd.)," *J. Roy. Statist. Soc.* **71**, 651–678 (1908).
56. T. Cover, J. Thomas, and J. Wiley, *Elements of Information Theory* (Wiley, 1991).
57. B. Frieden, *Physics from Fisher Information: a Unification* (Cambridge University, 1998).
58. D. Just and R. Bamler, "Phase statistics of interferograms with applications to synthetic aperture radar," *Appl. Opt.* **33**, 4361–4368 (1994).
59. J. Lee, K. Hoppel, S. Mango, and A. Miller, "Intensity and phase statistics of multilook polarimetric and interferometric SAR imagery," *IEEE Trans. Geosci. Remote Sens.* **32**, 1017–1028 (1994).
60. A. Ferretti, C. Prati, and F. Rocca, "Multibaseline InSAR DEM reconstruction: the wavelet approach," *IEEE Trans. Geosci. Remote Sens.* **37**, 705–715 (1999).
61. F. Lombardini, F. Gini, and P. Matteucci, "Application of array processing techniques to multibaseline InSAR for layover solution," in *Proceedings of the 2001 IEEE Radar Conference, 2001* (IEEE, 2002), pp. 210–215.
62. A. Ferretti, A. Monti-Guarnieri, C. Prati, F. Rocca, and D. Massonet, *InSAR Principles-Guidelines for SAR Interferometry Processing and Interpretation*, (ESA, 2007), Vol. 19, Chap. Part B.
63. J. W. Eaton, D. Bateman, and S. Hauberg, *GNU Octave Manual* (Network Theory, 2008).
64. B. Kampes, "MATLAB toolbox for InSAR," <http://enterprise.lr.tudelft.nl/doris/software/insarmatlab.tar.gz>.
65. B. Kampes and S. Usai, "Doris: the Delft object-oriented radar interferometric software," presented at the International Symposium on Operationalization of Remote Sensing, Enschede, The Netherlands, 16–20 August 1999.
66. T. Strozzi and U. Wegmüller, "Land subsidence in Mexico City mapped by ERS differential SAR interferometry," in

Proceedings of the IEEE 1999 International Geoscience and Remote Sensing Symposium (IEEE, 1999), pp. 1940–1942.

67. E. Cabral-Cano, T. H. Dixon, F. Miralles-Wilhelm, O. Diaz-Molina, O. Sanchez-Zamora, and R. E. Carande, “Space geodetic imaging of rapid ground subsidence in Mexico City,” *Geol. Soc. Am. Bull.* **120**, 1556–1566 (2008).
68. P. López-Quiroz, M. Doin, F. Tupin, P. Briole, and J. Nicolas, “Time series analysis of Mexico City subsidence constrained by radar interferometry,” *J. Appl. Geophys.* **69**, 1–15 (2009).
69. H. Friis, “Noise figures of radio receivers,” *Proc. IREE Aust.* **32**, 419–422 (1944).
70. J. W. Tukey, *Exploratory Data Analysis, Behavioral Science: Quantitative Methods* (Addison-Wesley, 1977).
71. E. Lehmann and G. Casella, *Theory of Point Estimation* (Springer, 1998).